Proof of Principle in a De novo Designed Protein Maquette: An Allosterically Regulated, Charge-Activated Conformational Switch in a Tetra-α-Helix Bundle[†]

Anne M. Grosset,[‡] Brian R. Gibney,[§] Francesc Rabanal,[||] Christopher C. Moser, and P. Leslie Dutton*

Johnson Research Foundation, Department of Biochemistry and Biophysics, University of Pennsylvania, Philadelphia, Pennsylvania 19104

Received October 30, 2000; Revised Manuscript Received February 13, 2001

ABSTRACT: New understanding of the engineering and allosteric regulation of natural protein conformational switches (such as those that couple chemical and ionic signals, mechanical force, and electro/chemical free energy for biochemical activation, catalysis, and motion) can be derived from simple de novo designed synthetic protein models (maquettes). We demonstrate proof of principle of both reversible switch action and allosteric regulation in a tetra-α-helical bundle protein composed of two identical di-helical subunits containing heme coordinated at a specific position close to the disulfide loop region. Individual bundles assume one of two switch states related by large-scale mechanical changes: a *syn*-topology (helices of the different subunits parallel) or *anti*-topology (helices antiparallel). Both the spectral properties of a coproporphyrin probe appended to the loop region and the distance-dependent redox interaction between the hemes identify the topologies. Beginning from a *syn*-topology, introduction of ferric heme in each subunit (either binding or redox change) shifts the topological balance by 25−50-fold (1.9−2.3 kcal/mol) to an *anti*-dominance. Charge repulsion between the two internal cationic ferric hemes drives the *syn*- to *anti*-switch, as demonstrated in two ways. When fixed in the *syn*-topology, the second ferric heme binding is 25−80-fold (1.9−2.6 kcal/mol) weaker than the first, and adjacent heme redox potentials are split by 80 mV (1.85 kcal/mol), values that energetically match the shift in topological balance. Allosteric and cooperative regulation of the switch by ionic strength exploits the shielded charge interactions between the two hemes and the exposed, cooperative interactions between the coproporphyrin carboxylates.

Early biochemical demonstrations of allosteric regulation of hemoglobin oxygen affinity by biphosphoglycerate (*1*), or of lac repressor DNA affinity by lactose (*2−4*), heralded the idea that protein conformational changes could allosterically couple distinctly different biological activities at remote sites across a protein. In recent years, we have seen direct demonstrations of structural changes accompanying the energy conversions of the proton driven ATP-synthase (*5, 6*), the cyt bc_1 complex (*7−10*) and molecular motors (*6*), chemical transformations of enzymatic catalysis (*11*), and the binding interactions of signal transduction and gene regulation (*12*). These conformational changes, driven by a variety of stimuli, many involving charge change (*13*), range from subtle structural alterations within a single protein, through larger subunit displacements or rearrangements within a larger complex, to conspicuous oligomeric reorga-

nizations. Large or small, the structural alterations often reach over considerable distances to couple a wide range of biological activities and their allosteric regulation. In this paper, we have explored the engineering and construction of a de novo designed protein maquette, greatly simplified in comparison to natural counterparts, that demonstrates internal chemical binding and charge interactions reversibly coupled to distinctive protein transformation of sufficient magnitude to function as a biological switch. The maquette also includes allosteric regulation of the switch.

The energetics of the switch, summarized in Figure 1, may be illustrated by a much-simplified view of the *Escherichia coli* lac repressor model of biochemical regulation (*2−4*). The repressor (**M**) adopts two structurally distinct conformational forms "a" and "b" that are influenced by lactose, the activating stimulus, **C**. Let us say that in the absence of lactose, the conformational equilibrium between a**M** and b**M** favors a**M**, while at levels of lactose sufficient to bind fully to the repressor protein the conformational equilibrium between a**MC** and b**MC** now favors b**MC**. With appropriately matched and balanced values of the conformational and binding equilibria, changes in concentration of lactate can switch the **M** conformational populations from virtually all "a" to virtually all "b". The sides of the square are defined by equilibrium interaction constants (K_{eq}). For the interaction of **C** with either the a**M** topologies or b**M** topologies, $K_{eq1} = [a\mathbf{M}][C]/[a\mathbf{MC}]$ and $K_{eq3} = [b\mathbf{M}][C]/[b\mathbf{MC}]$. Analogously, for the equilibrium constants between

‡ Current address: Department of Biochemistry and Molecular Biology, Georgetown University School of Medicine, 3900 Reservoir Road, 329 Basic Science Building, Washington, DC 20007.

§ Current address: 3000 Broadway, MC 3121, Department of Chemistry, Columbia University, New York, NY 10027.

|| Current address: Departament de Química Orgànica, Universitat de Barcelona, Martí i Franquès, 1-11. 08028 Barcelona, Espana.
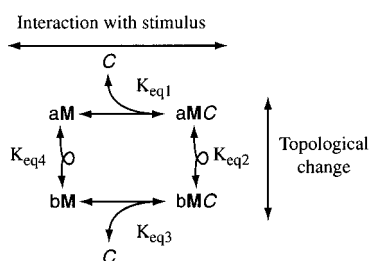
FIGURE 1: Model of a mechanical molecular switch. **M** is a protein that displays two distinct conformational or topological states a**M** and b**M** in equilibrium with each other. In the presence of **C**, a binding molecule or environmental condition or structural force specific to **M**, two additional states a**M**C and b**M**C enter the equilibrium creating the thermodynamic square shown. This square describes the equilibrium states of a molecular switch activated by changes in **C** that generate and control the appearance and disappearance of one or more specific conformational states of **M**. The amplitude of **C** relative to the equilibrium constants govern which of the state(s) dominate the mixture.

the two conformational states with and without **C**, $K_{eq2} =$ [b**M**C]/[a**M**C] and $K_{eq4} =$ [b**M**]/[a**M**]. Thus $K_{eq1}/K_{eq3} = K_{eq2}/K_{eq4}$. The difference of standard free energy of switching $(\Delta\Delta G^{\circ\prime}_{switch})$[1] for moving from state a**M** to b**M** in the absence of **C** as compared to the same change in the presence of **C** is given by

$$\Delta\Delta G^{\circ\prime}_{switch} = \Delta G^{\circ\prime}_4 - \Delta G^{\circ\prime}_2 = RT \ln[K_{eq2}/K_{eq4}] \quad (1a)$$

where R is the gas constant, and T is the absolute temperature. The corresponding difference of standard free energy of interaction between the states $(\Delta\Delta G^{\circ\prime}_{interaction})$ is the difference in moving from b**M**C to b**M** as compared to moving from a**M**C to a**M** given by

$$\Delta\Delta G^{\circ\prime}_{interaction} = \Delta G^{\circ\prime}_3 - \Delta G^{\circ\prime}_1 = RT \ln[K_{eq1}/K_{eq3}] \quad (1b)$$

The thermodynamic square drawn in Figure 1 requires that these $\Delta\Delta G^{\circ\prime}$ are equal.

$$\Delta\Delta G^{\circ\prime}_{switch} = \Delta\Delta G^{\circ\prime}_{interaction} \quad (1c)$$

In our lac example, a**M** has a high and specific affinity for DNA. The DNA bound state represents the repression of transcription of lactose metabolizing enzymes. The b states favored when lactose is bound (b**M**C) have a low affinity for DNA and so release the repressed transcription, through the connecting and scissors-like conformational motion in the repressor.

It is relatively rare for a biological system to permit the measurement of all the equilibrium constants of thermodynamic schemes similar to Figure 1. With the opportunity for the construction of families of related synthetic maquettes, these complete thermodynamic measurements become more feasible. Our maquette designs continue to draw inspiration from the minimal approach (14) and the guidelines established for the synthesis of stable, folded proteins (15−17).
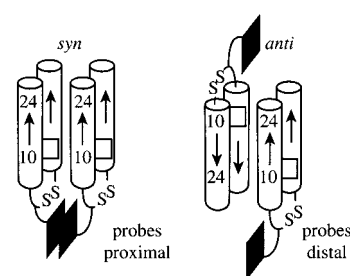
FIGURE 2: Proposed topologies of tetra-α-helical bundle protein maquettes. The macroscopic dipoles (arrows) of the two helices within the α-ss-α subunits are parallel in both cases but the α-ss-α subunits assemble to form the (α-ss-α)$_2$ with either a *syn*- or *anti*-topology or conformation. In the *syn*-topology, the external probes, coproporphyrin, or pyrene are proximal, and thus capable of forming coproporphyrin dimers or pyrene excimers. In the *anti*-topology, the external probes are distal, and thus remain in monomeric form. Similarly, in the *syn*-topology, the two bis-histidine (10,10′ positions of each α-ss-α subunit) bound hemes (protoporphyrin IX) are proximal, and thus capable of participating in charge interactions, while in the *anti*-topology the hemes are distal and electrostatic interactions are expected to be much weaker. In this series of protein maquette variants, the 24, 24′ positions of each α-ss-α subunit are filled by alanine or serine.

The maquette design we develop here is based on tetra-α-helix bundles composed of two identical di-α-helical monomer subunits as shown schematically in Figure 2 (18). Each di-α-helical monomer is constructed with two parallel helices linked by a disulfide bond to form α-ss-α. These assemble in solution to form highly associated homodimeric (α-ss-α)$_2$ tetra-α-helical bundle structures. Figure 2 also demonstrates that, in principle, the subunits can assemble in either of two distinctly different conformational states, best described in terms of their *syn*- and *anti*-topologies (19). The *syn*- and *anti*-topologies of the (α-ss-α)$_2$ serve our purpose in representing the "a" and "b" states of **M**. Thus, for our protein, the structural transformations K_{eq2} and K_{eq4} of eq 1a and Figure 1 specify the topological equilibrium:

$$K_{anti-syn} = [anti]/[syn] \quad (2)$$

We choose heme (iron protoporphyrin IX) as the activating source, **C**, for our maquette design, **M**, for several reasons. Histidines at internal positions of each α-ss-α provide a defined locus for bis-histidine axial ligation of one heme per subunit, and it follows that a total of two hemes can be bound per (α-ss-α)$_2$ as shown schematically in Figure 2. The histidine ligation also provides a clearly identifiable spectroscopic signature for heme binding and for its individual redox states. The hemes offer two ways to act on (α-ss-α)$_2$ to alter the *syn*- and *anti*-topology ratio that are biologically relevant and energetically significant. In the first case, steric hindrance between hemes binding to (α-ss-α)$_2$ in the *syn*-topology (hemes proximal) (20) but not in the *anti*-topology (hemes distal) may destabilize the *syn*-topology and favor a shift to the *anti*-topology. In the second case, and the principle reason for selecting heme, the formal uncharged ferrous state when reduced and the cationic charged ferric state when oxidized raise the possibility that simple redox modulation and accompanying charge repulsion may influence the *syn-anti*-equilibrium. Thus, when two cationic ferric hemes are bound in the interior of (α-ss-α)$_2$ to create diferric-heme (α-ss-α)$_2$, charge repulsion may favor a shift from *syn*-topology (hemes proximal) to *anti*-topology (hemes distal).

In this case, either the binding of two ferric (but not ferrous) hemes, or a change in the environmental oxidation−reduction potential that oxidizes the hemes, would shift the equilibrium from *syn*- toward *anti*-topology. Thus, for our protein, the general equilibria K_{eq1} and K_{eq3} of eq 1b and Figure 1 can be measured as differences in the ferric-heme binding titrations or in redox potentials.

It is clear from Figure 2 that to facilitate relaxation of steric hindrance or charge repulsion between two adjacent hemes in a *syn*-topology, the heme binding site should be placed asymmetrically along a helix of sufficient length. The prototype (α-ss-α)$_2$, previously called H10A24 (*18*) and here called A24-(α-ss-α)$_2$, satisfies this basic requirement. The helical segments of the α-ss-α subunits include about 27 residues and the histidines placed at positions H10 and H10′, well toward the loop region end. In this arrangement, the distance between the hemes changes significantly in moving from *syn*-topology [where hemes are apparently in near van der Waals contact, Fe−Fe distance about 13 Å (*20*)] to *anti*-topology (where the hemes are well separated, Fe−Fe distance estimated at about 26 Å).

It is more challenging to establish the appropriate initial poise of *anti-syn*-ratio prior to heme binding or oxidation (*21*). To be an effective switch, the maquette must be engineered with an initial *anti-syn*-ratio suitably below unity. How far below unity depends on how much energy difference is available in the heme steric hindrance or the charge repulsion. Clearly, the steric or charge effects must be sufficient to change the ratio from suitably below, to suitably above, unity to realize a significant switch from *syn*- to *anti*-topology. For instance, the realization of an *anti-syn*-ratio switch from <0.1 to >10, and hence a $\Delta\Delta G^{\circ\prime}_{switch}$ of >2.7 kcal/mol, will require a matching $\Delta\Delta G^{\circ\prime}_{interaction}$ exerted by the heme to promote the change from the *syn*- to the *anti*-topology, according to eq 1.

Earlier biochemical studies have established that the subunits of prototype A24-(α-ss-α)$_2$ are poised toward the desired *syn*-side of the equilibrium as shown on the left of Figure 2 (*19*, *22*). However, work with A24-(α-ss-α)$_2$ and H24-(α-ss-α)$_2$ (previously called H10H24) has shown that neither steric hindrance from added hemes nor the charge states of the ferric heme are great enough to force an *anti*-topology (*23*). Redox titrations of the diheme A24-(α-ss-α)$_2$ reveal a pronounced 75 to 100 mV splitting in the potentials of the two hemes, consistent with the presence of significant charge repulsion in a firmly *syn*-topology. Such redox splitting could effect a 20−50-fold change in the *anti-syn*-ratio (eq 1). Clearly, the initial *anti-syn*-ratio of the A24-(α-ss-α)$_2$ is too small to be an effective switch. It follows then if we are to meet design criteria, the initial *ant-syn*-ratio of the (α-ss-α)$_2$ needs to be about 0.1 so that the impact of the 20−50-fold change from charge repulsion can be observed as a substantial switch in topology.

Quantitative predictions regarding the equilibrium poise of topological populations in assemblies typified by (α-ss-α)$_2$ remain a very uncertain exercise (reviews in refs *15* and *16*). For our present design, we have drawn on our own experience. We have found that the simple exchange of the internal alanine for serine at position 24 of each α-helix produces S24-(α-ss-α)$_2$ with a topology apparently already dominated by the *anti*-form (*19*) shown on the right of Figure 2. While an initial *anti*-topology obviously does not satisfy

our engineering requirements, the opportunity existed in the *anti*-S24-(α-ss-α)$_2$ structures to make use of coproporphyrin (CP) pendants on the loop regions of each α-ss-α subunit (see Figure 2) to adjust the *anti-syn*-ratio toward a more suitable initial value smaller than unity. While CP appended to the loop region has been used primarily as a topological probe, it has been estimated (*23−25*) that it would confer an estimated 10−100-fold shift from an *anti*- toward a *syn*-topology because of a tendency of CP free in solution to form a cofacial dimer. Appended CP has an additional potentially useful way of adjusting the *anti-syn*-ratio through its three anionic carboxylate charges on the periphery of each macrocycle. It is reasonable to consider that these multiple anionic charges will oppose CP dimer formation in solution in a manner that should be modulated, possibly cooperatively, by ionic strength. In this way, ionic strength modulation of CP dimerization may provide some engineering tolerance to the uncertain initial value of the *anti-syn*-ratio of S24-(α-ss-α)$_2$ and provide a measure of control over it to optimize the heme activated topological switch. Thus, positioned remote from the hemes and their binding site, CP presents us with a potential allosteric regulator of the switch.

EXPERIMENTAL PROCEDURES

Chemicals and Solvents. Chemicals and solvents used in the synthesis and purification were of the highest available grade and purchased from the following suppliers: NovaSyn PR-500 resin from Calbiochem-Novabiochem (La Jolla, CA); Fmoc-protected amino acid pentafluorophenyl esters from PerSeptive Biosystems (Framingham, MA) with the exception of Fmoc-L-Arg(Pmc)-OPfp from Bachem (King of Prussia, PA); 1,2-ethanedithiol from Fluka (Ronkonkoma, NY); and iron protoporphyrin IX (hemin) from Porphyrin Products Inc. (Logan, UT.)

Peptide Synthesis. Solid-phase synthesis with Fmoc/^{t}Bu chemistry (base-labile 9-fluorenylmethoxycarbonyl-amino acids with acid-labile *tert*-butyl-based side chain protecting groups where necessary) was used to synthesize all peptides as described in (*18*), which were then purified by reversed phase C$_{18}$ HPLC, and characterized by analytical HPLC. The resulting peptide identities were confirmed by laser desorption mass spectrometry. FPLC was used to purify peptides and to establish that all of the assembled *apo*- or *holo*-proteins used in these studies were the appropriate molecular weight for tetra-α-helix bundles. The designs used in the present work were closely related to a prototype from previous work (*18*), then called H10A24. This protein was built from four identical 31 amino acid peptides (α-SH): *Ac*-CGGGELWKL__**H**EELLKK__FEELLKL__**A**EERLKK__L-*CONH*$_2$.

Two of these (α-SH) helices were linked by a disulfide bond in the loop region, αssα, which spontaneously formed a tetra-α-helix bundle, (α-ss-α)$_2$. The histidines at positions 10,10′ of each α-ss-α equipped the (α-ss-α)$_2$ to bind up to two bis-histidine ligated hemes. This protein maquette was used (a) without further change but with a new name of A24-(α-ss-α)$_2$ and (b) with a substitution of the alanine at 24 in each helix for serine and called S24-(α-ss-α)$_2$.

Protein Concentrations. These were determined in a UV/VIS Perkin-Elmer Lambda 2 spectrophotometer at ambient temperature using quartz cells of 1.0 cm path length. A24-
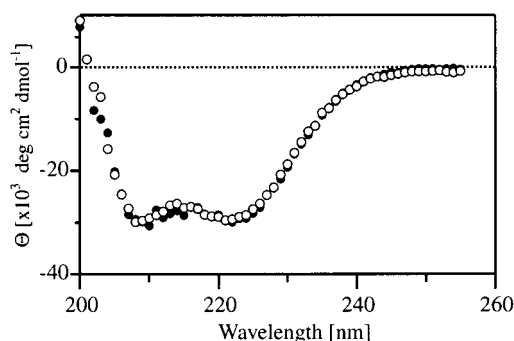
FIGURE 3: Circular dichroism of S24- and A24-(α-ss-α)$_2$ protein maquettes. Circular dichroism spectra of S24- (open circles) and A24-(α-ss-α)$_2$ (closed circles). Mean residue ellipticity [Θ]$_{222}$ is plotted against wavelength (nm). Protein concentration is 8 μM and the solution is 10 mM phosphate buffer at pH 8.

or S24-(CP-α-ss-α)$_2$ concentrations were determined by tryptophan absorbance at 280 nm with an extinction coefficient of 5700 M^{-1} cm^{-1} (*26*).

Attachment of Optical Probes Pyrene and Coproporphyrin. Pyrenated derivatives of A24-(α-ss-α)$_2$ and S24-(α-ss-α)$_2$ were prepared by reacting 1-pyrene butyric acid/1,3-diisopropylcarbodiimide/1-hydroxybenzotriazole (1:1:1) with the N-terminal amine of cysteine of the α-helix peptide (α-SH) for 2 h. This was then cleaved with trifluoroacetic acid/1,2-ethanedithiol/water (92:6:2) to form the pyrene derivative (pyr-α-SH) (*19, 23−25, 27*). Pyr-α-SH was then heterodimerized with the acetylated version of the unpyrenated α-SH using the pNPys derivitization technique (*25*) to yield A24- or S24-(pyr-α-ss-α), which spontaneously associated into A24- or S24-(pyr-α-ss-α)$_2$. Coproporphyrin (CP) derivatives were prepared similarly to yield A24- or S24-(CP-α-ss-α)$_2$. Proteins containing pyrene or coproporphyrin pendants are subject to photochemical deterioration when exposed to light in the presence of oxygen, so storage in the dark under an inert atmosphere at −20 °C was standard procedure.

Solution Molecular Weight Determination. A Beckman System Gold HPLC was used for gel filtration chromatography using a calibrated Supelco GFC-100 column (7.5 × 300 mm) equilibrated with 50 mM Tris-HCl buffer with 100 mM NaCl, pH 8.5, at a flow rate of 0.5 mL/min. All proteins were established as tetra-α-helix bundles of the (α-ss-α)$_2$ type with little or no other oligomeric, (α-ss-α)$_n$, structures.

Circular Dichroism Spectrophotometry. CD spectra were measured on an AVIV 62 DS spectropolarimeter using rectangular quartz cells of 0.2 and 1.0 cm path length. Temperature was controlled with a thermoelectric module, combined with a Neslab CFT-33 refrigerated circulating water bath as a heat sink. Protein concentrations were around 10 μM as determined spectrophotometrically using $\epsilon_{280} = 5700$ mol^{-1} cm^{-1} helix^{-1} for Trp. Figure 3 shows that S24-(α-ss-α)$_2$ displays quite similar circular dichroism spectra to the previously characterized A24-(α-ss-α)$_2$ (*18, 21*), indicating that both possess a secondary structure comprising more than 80% helicity (more than 26 000 -[Θ]$_{222}$ deg cm^2 dmol^{-1} as compared to 32 000 -[Θ]$_{222}$ deg cm^2 dmol^{-1} for 100% helicity). Spectra (not shown) obtained for A24-(pyr-α-ss-α)$_2$ and S24-(pyr-α-ss-α)$_2$ and for the heme containing S24-(α-ss-α)$_2$ were similar. S24-(α-ss-α)$_2$ showed the same

order of resistance to thermal denaturation as A24-(α-ss-α)$_2$ (not shown). Thus, the replacement of alanine by serine at position 24 in each helix altered neither helical content nor the coiled-coil character.

Iron Protoporphyrin IX Binding. Dissociation constants (K_d values) for heme and protein were determined as before (*18, 28*). A freshly prepared solution of iron protoporphyrin IX (hemin typically in the ferric form) in spectrophotometric grade dimethyl sulfoxide was added in 1 μL (0.1−0.2 heme/binding site) increments to the solution of *apo*-protein (1 to 2 mL of 0.1 to 3 μM protein in 50 mM Tris buffer, 100 mM NaCl at pH 8.5). The final concentration of dimethyl sulfoxide to buffer solution was ≤0.5%. When ferrous protoporphyrin IX was added to the apo-protein, both the apo-protein and the protoporphyrin IX solutions were poised at a redox potential below −180 mV in an anaerobic cuvette usually used for redox potentiometry (see below). When single hemes were added per tetra-α-helix bundle to produce monoheme A24-(α-ss-α)$_2$ or monoheme S24-(α-ss-α)$_2$, there is the probability of realizing significant statistical populations of double occupancy. Mathematical modeling at the experimental concentrations used demonstrates at least for one ferric heme added to A24-(α-ss-α)$_2$ double occupancy will be below 10% because of the large difference in the heme dissociation constants for the first heme and the second heme added (*18, 29*). However, for the presence of ferrous heme or for one ferric heme added to S24-(α-ss-α)$_2$ the K_d values for the first and second hemes ligated at the 10,10′ histidine sites are indistinguishable, and so in these cases the double occupancy at an overall one heme per (α-ss-α)$_2$ will be as much as 25%.

Redox Potentiometry. Redox potentiometry (*30*) was done in combination with UV−vis absorption spectra (Perkin-Elmer Lambda 2). Freshly made and argon-degassed sodium dithionite or potassium ferricyanide solutions (in 100 mM NaCl, 50 mM Tris-HCl buffer at pH 8.5) were used to adjust the solution redox potential monitored with a platinum measuring electrode and a saturated KCl calomel reference electrode. All the potentials reported in the text are referred to the standard hydrogen electrode. The redox mediators used to promote equilibrium between electrode and the protein bound heme were carefully selected to cover the range of the potentiometric titration from +50 to −400 mV, and to interfere as little as possible with the monitoring of the reduced α- and γ-bands of the bound heme. The redox mediators were as follows: 20 μM duroquinone, 10 μM pyocyanine, 10 μM 2-hydroxy-1,4-naphthoquinone, 1 μM indigocarmine, 10 μM anthraquinone-2-sulfonate, 1 μM phenylsafranine, and 2 μM benzyl viologen. Heme protein solutions were transferred to a previously argon-degassed buffer solution in a flowing argon blanketed anaerobic cuvette for redox potentiometry with a 1 cm path length, yielding a final heme protein concentration of approximately 5 μM in a total solution volume of 5 mL. The solution was degassed for a further 30 min while protected from light prior to starting the redox titration. Cuvette solution temperature was controlled with water at 22 °C circulating through the cuvette holder. Redox equilibrium was established within 2−3 min.

The fraction of heme protein maquette reduced was analyzed by the appearance of the typical α-band of the ferrous bis-histidine heme at 560 nm using a 575 nm

reference wavelength. This analysis was also confirmed with the γ-band of ferrous bis-histidine heme at 426 nm. Redox midpoint potential values at pH 8.5 ($E_{m8.5}$) were obtained from the fraction of heme reduced plotted against the redox potential, E_h, and fitted to the Nernst equation:

$$E_h = E_{m8.5} + RT/nF \ln [ox]/[red] \tag{3a}$$

where n is the number of electrons participating in the redox reaction, F is the Faraday constant, and [ox] and [red] are the optically assayed concentrations of oxidized and reduced species, respectively. Analysis of the titration was routinely followed using a fit for one $n = 1$ or for two $n = 1$ redox transitions. The corresponding standard free energy change of oxidation and reduction relative to the standard hydrogen electrode (SHE conventionally set to 0 V) is

$$\Delta G°\,' = -nE_{m8.5}F \tag{3b}$$

Topological Probes of the (α-ss-α)$_2$ Maquettes. Three different methods were used to characterize topological conformation of the (α-ss-α)$_2$. Two methods employed optical probes, pyrene (*27*) and coproporphyrin (*23*), placed as external pendants on the central cystine amides in the flexible GGGCCGGG loops of each α-ss-α as described above and shown in Figure 2. The possibility that the probes enter the interior of the (α-ss-α)$_2$ structure rather than staying in solution as designed was tested by examination for the expected hindrance of heme binding; none was observed. Moreover, we find that pyrene and CP exhibit similar spectral properties whether covalently attached to the heme protein maquette or free in buffer solution, indicating that after attachment the chromophores remain in full contact with the supporting aqueous medium. In the case of CP, the three peripheral anionic propionate groups strongly favor this situation. The third method to determine topology took advantage of the electrostatic interactions between hemes contained within the low dielectric interior of the bundle (*18, 20, 30*). The foundations of the three methods are outlined below.

Anti-Syn-Ratios from Pyrene Monomer$-$Excimer Fluorescence. The fluorescence emission spectra of A24- or S24-(pyr-α-ss-α)$_2$ maquettes were measured on a Hitachi F-2000 fluorescence spectrophotometer using a cuvette of 1 cm path length. Excitation wavelength was at 350 nm. Measurements were done in 10 mM potassium phosphate buffer/dimethyl sulfoxide (4:1 v/v) at pH 7.0 bubbled with argon for at least 15 min before adding protein (15 μM) and maintained thereafter under an atmosphere of argon (*27*).

Pyrene is well-known to form a cofacial excimer when two pyrenes are located less than about 4 Å from one another and excited by light at around 350 nm (*31$-$33*). The resulting pyrene excimer displays characteristic fluorescence distinct from the pyrene monomer fluorescence. However, since the pyrene excimer is stable only in the excited state and depends on the collision frequency of the adjacent pyrenes, the pyrene excimer band at 480 nm is usually accompanied by monomer fluorescence at 380 and 400 nm. Pyrene excimer fluorescence has been successfully used as a probe of helix$-$helix proximity and protein conformational change (*34$-$36*) or to resolve parallel/antiparallel orientation in leucine zipper homodimers (*27*). In these apo-protein systems, observation

of pyrene-excimer fluorescence indicates pyrenes in close proximity, and thus implies *syn*-topology. However, observation of excimer fluorescence cannot be used to quantitatively determine *syn*-topology since it reflects only the portion of the photoexcited pyrenes that after collision adopt the right configuration to form the excimer. Thus, pyrene provides an underestimation for the actual proportion of pyrenes in close proximity to one another and hence the *syn*-topology population. Apart from unproductive collisions clouding quantification, the pyrene is prone to fluorescence quenching from many redox cofactors including hemes, so this restricts the method to the apo- forms of the proteins. On the other hand, enhancement of the excimer fluorescence can arise from nonspecific aggregation of proteins induced by the hydrophobic pyrene (*27, 37*); this possibility was minimized by working in the 10$-$15 μM range.

Anti-Syn-Ratios from Coproporphyrin Monomer$-$Dimer UV$-$Vis Spectra. CP readily forms a cofacial dimer when two CP are proximal. The CP-dimer displays a characteristic Soret absorption band at 372 nm clearly distinguishable from the monomer band at 394 nm (*23$-$25*). Figure 4, panel A, depicts a trifluoroethanol (TFE) titration of S24-(CP-α-ss-α)$_2$. TFE separates the (CP-α-ss-α) monomers resulting in a change of the CP-dimer spectrum for the (CP-α-ss-α)$_2$ to the CP-monomer spectrum for the (CP-α-ss-α) (*38*). In a dimeric (CP-α-ss-α)$_2$ bundle, a CP-dimer spectrum indicates *syn*-topology and CP-monomer indicates *anti*-topology. In the case of the heme containing (CP-α-ss-α)$_2$ proteins where there is significant overlap between the dimer and monomer absorption bands for the CP and the oxidized and reduced bands for the bound heme, errors in estimation of the concentrations of CP-monomer and bound heme were minimized by global spectral deconvolution. Deconvolution of the spectra was achieved by iterative fitting of a simple summation of the individual spectra of CP dimer and monomer and ferrous and ferric hemes as shown in spectra a$-$d of Figure 4, panels B and C.

In using CP as a probe, the intrinsic tendency of CP to self-associate and the influence it has on the topology of the structures has been recognized (*23, 24, 38*). The monomer-to-dimer transition of coproporphyrin (CP) has two components. The first is the formation of cofacial dimers by macrocycle interactions which has been estimated to be at least 1.5$-$2 kcal/mol at high ionic strength ($\sim$150 mM KCl). The second is the charge interaction between the three peripheral propionates on each coproporphyrin that is expected to oppose formation of cofacial dimers in a way modulatable by solution ionic strength.

Anti-Syn-Ratios from Redox Charge Interactions Between Hemes. Hemes are bis-histidyl ligated to each of the α-ss-α subunits of the (α-ss-α)$_2$ and used as a topological probe by making use of the electrostatic interactions between the two hemes placed in the interior of the (α-ss-α)$_2$ measured by redox potentiometry. Charge interactions between two hemes, seen as a splitting in their potentials by as much as 100 mV has been measured for A24-(α-ss-α)$_2$ (*18*). It was reasoned that such a value for two hemes less than 13 Å apart (Fe to Fe) could only be accommodated if the hemes were interacting through a low dielectric interior of the bundle with a *syn*-topology (*20*). On the other hand, charge interactions along the greater distance of around 26 Å along the axis of the bundle when in the *anti*-topology would be predicted to
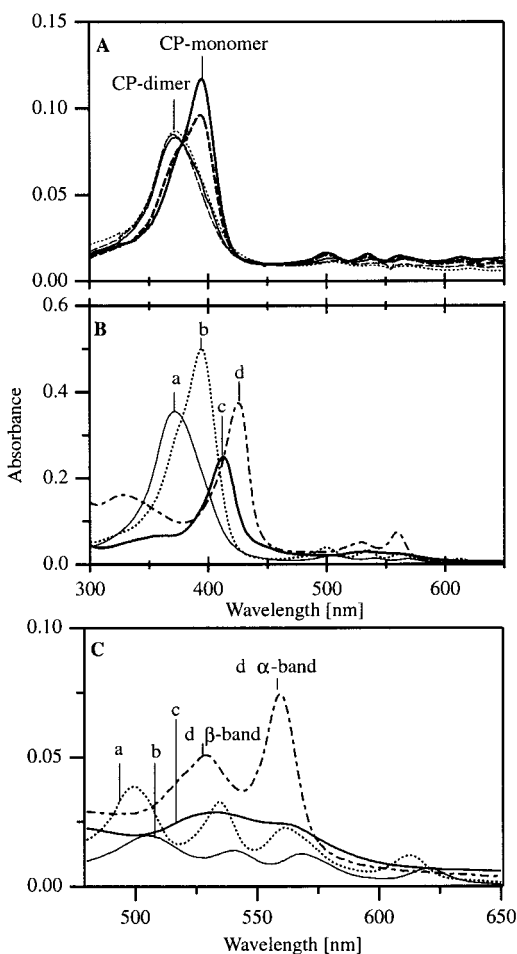
FIGURE 4: Absorption spectra of S24- or A24-(CP-α-ss-α)$_2$ used for deconvolution of *anti-syn*-topology determination and heme binding titrations. (A) Absorption spectra of S24-(CP-α-ss-α)$_2$ without heme at approximately 5 μM in 100 mM NaCl 50 mM Tris-HCl buffer pH 8.5 with various percentages (0, 11, 20, 27, and 33% vol/vol) of trifluoroethanol (TFE) added at 22 °C. The absorption maximum for the CP-dimer is at 372 nm (0% TFE) and that for the CP-monomer is at 394 nm (33% TFE). (B) Absorption spectra of individual spectral components used in deconvolution of ferrous and ferric hemes and CP monomers and dimers A24-(CP-α-ss-α)$_2$ and S24-(CP-α-ss-α)$_2$. The proteins are present at approximately 2 μM in the buffer as described above. Spectrum a is the CP-dimer in S24-(α-ss-α)$_2$ as described in panel A at 0% TFE. Spectrum b is the CP-monomer in S24-(CP-α-ss-α)$_2$ as described in panel A at 33% TFE. Spectrum c is S24-(α-ss-α)$_2$ with two bound bis-histidyl ferric hemes. Spectrum d is S24-(α-ss-α)$_2$ with two bound bis-histidyl ferrous hemes. (C) Magnification of the α and β bands of the absorption spectra.

result in less than 5 mV of electrostatic interaction (*18, 20, 39*). This electrochemical probe draws upon charge interactions between the hemes which also influence the *anti-syn*-ratio and must be accounted for.

The method is based on potentiometric assay of redox heterogeneity resulting from charge interactions in *syn*-oriented diheme (α-ss-α)$_2$ structures. The sensitivity of this method can be undermined by heterogeneity that arises from other environmental sources, perhaps associated with variable heme binding to the (α-ss-α)$_2$ structures. As a foundation for these measurements, we have examined for such heterogeneity by potentiometrically following the course of oxidation−reduction for *single* hemes in A24-(α-ss-α)$_2$ and S24-(α-ss-α)$_2$. Figure 5 shows that the oxidation−reduction titration of a single heme in both A24-(α-ss-α)$_2$ (a, filled
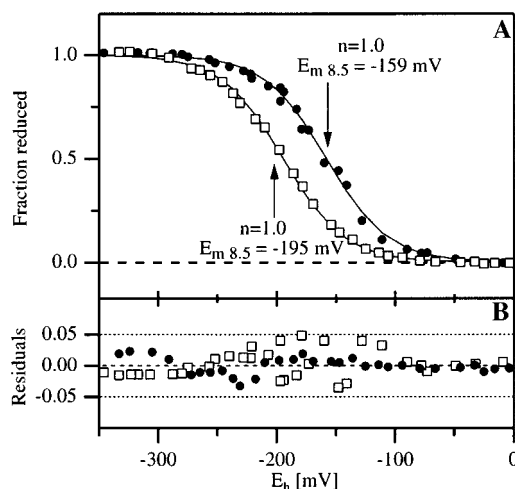
FIGURE 5: Redox titrations of monoheme A24-(α-ss-α)$_2$ and monoheme S24-(α-ss-α)$_2$. (A) Redox titrations of (a) monoheme A24-(α-ss-α)$_2$ (closed circles) and (b) monoheme S24-(α-ss-α)$_2$ (open squares) at concentrations of approximately 5 μM. Titrations were performed at pH 8.5 in 100 mM NaCl, 50 mM Tris-HCl buffer at 22 °C. The fraction heme reduced is plotted as a function of the ambient redox potential (mV). Data are shown from a titration in the reductive direction; identical results were obtained for the oxidative direction, demonstrating rapid equilibrium and reversibility. The reduction of the heme was monitored by optical measurement of the α-band and confirmed by the Soret band of the reduced form (not shown), as both measurements produced the same result. The fraction reduced was calculated from the differential absorbance between the α band at 558 nm and a reference wavelength at 575 nm. Monoheme A24-(α-ss-α)$_2$ has an $E_{m8.5}$ value of −158 mV. The standard deviation was 7 mV for $N = 3$, and the reduced χ_ν^2 ("goodness of fit") was 0.0007 with probability $P_\chi \geq 0.95$ for the titration depicted. Monoheme S24-(α-ss-α)$_2$ has an $E_{m8.5}$ of −195 mV. Here the standard deviation was 7 mV for $N = 2$ with a reduced χ_ν^2 of 0.0005 and probability $P_\chi \geq 0.98$ for the titration depicted. (B) Residuals of fraction heme reduced from a fit of a single Nernst equation to $n = 1.0$. Monoheme A24-(α-ss-α)$_2$ is represented by the black circles, and Monoheme S24-(α-ss-α)$_2$ by the open squares. The dotted lines indicate limits of ± 5%.

circles) and S24-(α-ss-α)$_2$ (b, open squares) was readily reversible and closely followed a single Nernst transition with an *n* value of 1.0. The figure also shows the residuals to the fits to the Nernst equation for $n = 1$ of these data. Nearly all data points fall within the ± 5% range with no apparent systematic trends suggestive of multiple conformations or a distribution of electrochemical states. These results demonstrate usefully homogeneous heme binding environments for the single hemes in the individual A24- and S24-(α-ss-α)$_2$ maquettes and hence provide a firm foundation for the use of the method as a topological probe. Thus, *syn*-oriented diheme (α-ss-α)$_2$ structures displaying ∼100mV splitting of the heme potentials, as opposed to *anti*-oriented diheme (α-ss-α)$_2$ structures displaying an undetectable level of splitting, should be readily quantifiable above the 5% limit.

RESULTS

Pendent Pyrene as a Probe for Syn- and Anti-Topology of A24- and S24-(pyr-α-ss-α)$_2$. Figure 6 shows the fluorescence spectra of the *apo*-forms of A24-(pyr-α-ss-α)$_2$ and S24-(pyr-α-ss-α)$_2$. A24-(pyr-α-ss-α)$_2$ (dashed line) shows a broad band at 480 nm typical of pyrene excimer fluorescence. The high excimer/monomer fluorescence ratio of 0.97
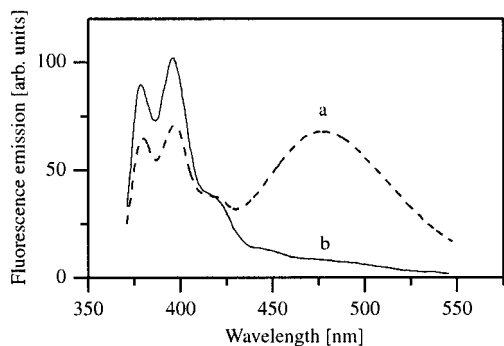
FIGURE 6: Fluorescence spectra of (pyrene-α-ss-α)$_2$. Fluorescence spectra of A24-(pyr-α-ss-α)$_2$ (dashed line) and S24-(pyr-α-ss-α)$_2$ (solid line) at approximately 15 μM. The excitation wavelength was at 350 nm in argon-degassed 10 mM potassium phosphate buffer/dimethyl sulfoxide (4:1 v/v) at pH 7.0. Excimer fluorescence in A24-(pyr-α-ss-α)$_2$ appears at 480 nm.

for A24-(pyr-α-ss-α)$_2$ indicates a high collision frequency of the pyrenes on each of the pyr-α-ss-α subunits and hence a close proximity. This suggests that *apo*-A24-(pyr-α-ss-α)$_2$ adopts a dominant *syn*-topology. In contrast, the *apo*-S24-(pyr-α-ss-α)$_2$ (solid line) has an excimer/monomer fluorescence ratio of only 0.08, suggesting a greater distance between the pyrenes (lower collision frequency) and a higher probability that S24-(pyr-α-ss-α)$_2$ is predominantly *anti*-topology. The pyrene suggests that the difference in the *anti-syn* ratio on substituting a serine for the alanine at position 24 is at least 12-fold. Further tests made on the heme containing (pyr-α-ss-α)$_2$ structures were prohibited by strong quenching of the pyrene fluorescence by heme.

Redox Potentiometry as a Probe for Syn- and Anti-Topology of A24-(α-ss-α)$_2$ and S24-(α-ss-α)$_2$. Figure 7, panel A, shows redox titrations of two hemes in A24-(α-ss-α)$_2$ and S24-(α-ss-α)$_2$. Diheme A24-(α-ss-α)$_2$ displays two equal, well-resolved, readily reversible redox transitions with $E_{m8.5}$ values at −246 and −170 mV and both fitting an n value of 1.0 (closed circles). The splitting of the potentials of the two hemes by approximately 76 mV confirms the earlier work (*18*) and the suggestion that the two hemes within the A24-(α-ss-α)$_2$ structure are proximal and hence that the two (α-ss-α) subunits of diheme A24-(α-ss-α)$_2$ adopt a *syn*-topology. This result is consistent with the above results for the apo A24-(pyr-α-ss-α)$_2$, and hence the A24 *syn*-topology appears insensitive to the presence of two hemes and independent of the redox state. In contrast, a similar redox titration of the two hemes of diheme S24-(α-ss-α)$_2$ displays a single transition with an n value of 1.0 (open squares). The two hemes in S24-(α-ss-α)$_2$ therefore both have $E_{m8.5}$ values, within experimental error, of −207 mV and similar to that obtained for a single heme (Figure 5). These results are again consistent with the data from the apo-S24-(pyr-α-ss-α)$_2$ analysis, and suggest that the two hemes in the S24-(α-ss-α)$_2$ are physically distal and that the two (α-ss-α) subunits adopt an *anti*-topology. Detailed quantitative analysis of the diheme redox transitions of A24- and S24-(α-ss-α)$_2$ as seen in Figure 7 again demonstrates that the amount of *anti*-topology in the *syn*-dominated diheme A24-(α-ss-α)$_2$ is less than 5% and conversely the amount of *syn*-topology in the *anti*-dominated diheme S24-(α-ss-α)$_2$ is also minor, less than 5%. These results translate into *anti-syn*-ratios of ≤0.05 for diheme A24-(α-ss-α)$_2$, and ≥20 for
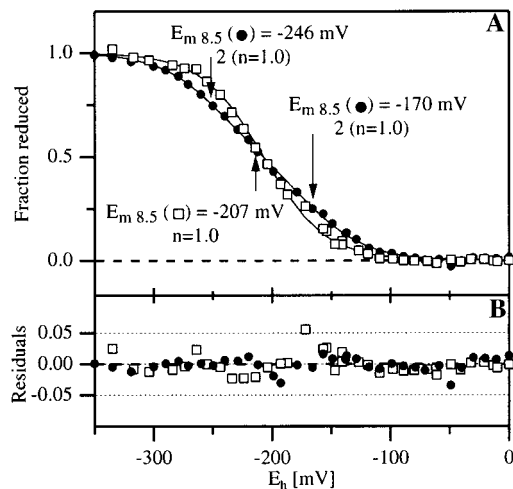
FIGURE 7: Redox titrations of diheme A24- and S24-(α-ss-α)$_2$. (A) Redox titrations of (a) diheme A24-(α-ss-α)$_2$ (closed circles) and (b) diheme S24-(α-ss-α)$_2$ (open squares) at concentrations of approximately 5 μM. Titrations were performed at pH 8.5 in 100 mM NaCl, 50 mM Tris-HCl buffer at 22 °C. The fraction heme reduced is plotted as a function of the ambient electrochemical potential (mV) in reductive titration (which exhibits reversibility upon oxidation). The redox state of the two hemes was monitored by optical measurement of the reduced form of the α-band and Soret-band (not shown); as both measurements produced the same result. The percent reduced was calculated from the differential absorbance between the α band at 558 nm and the reference absorbance at 575 nm. The A24 displays two $E_{m8.5}$ of −169 and −246 mV, with a standard deviation of 6 mV for $E_{m18,5}$ and 6 mV for $E_{m28,5}$ with $N = 3$. There is a reduced χ_v^2 of 0.0024 with probability $P_\chi \geq 0.99$ for the titration depicted. The S24 has an $E_{m8.5}$ of −207 mV with a standard deviation of 6 mV for $N = 3$ and a reduced χ_v^2 of 0.0092 with probability $P_\chi \geq 0.90$ for the titration depicted. (B) Residuals of fraction heme reduced from a fit of the Nernst equation to two times $n = 1$ for diheme A24-(α-ss-α)$_2$ (black circles) and a single $n = 1$ for diheme S24-(α-ss-α)$_2$ (open squares). The dotted lines indicate limits of ± 5%.

diheme S24-(α-ss-α)$_2$, extending the difference limit reported by pyrene to greater than 400-fold.

The work so far has been done at relatively high ionic strength (100 mM NaCl, 50 mM Tris-HCl buffer at pH 8.5) that is expected to screen any charge interactions that are accessible to the ions of the external aqueous phase. If the two hemes of A24-(α-ss-α)$_2$ are partly exposed to the external aqueous phase, then lowering the external ionic strength may increase the charge interactions between the adjacent ferric hemes and push the *anti-syn*-ratio up toward the *anti*-conformation and into the measurable range (i.e., ≥0.05). The effect of ionic strength on the charge interaction between the two hemes in A24-(α-ss-α)$_2$ is shown by comparing the titration in Figure 7 done at high ionic strength with that in Figure 8 done at lower ionic strength (10 mM Tris-HCl, pH 8.5). The redox titration done at the low ionic strength follows a similar course as found at high ionic strength, displaying two transitions of equal proportions and similar $E_{m8.5}$ values and splitting. Hence, at the lowered ionic strength, diferric-heme A24-(α-ss-α)$_2$ remains ≥95% in the *syn*-topology and the *anti-syn*-ratio ≥20. It follows therefore that the irons of the two proximal hemes of A24-(α-ss-α)$_2$ are solvent-protected and consequently electric field forces between the cationic charges of the two ferric hemes are internal and not alterable by the ionic strength of the external buffer solution.
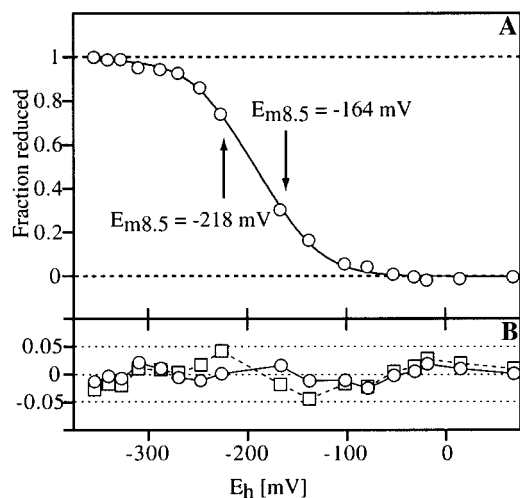
FIGURE 8: Redox titrations at low ionic strength of diheme A24-(α-ss-α)$_2$. Apart from the buffer solution which was 10 mM Tris at pH 8.5, all other conditions and analyses were as described in Figure 7. (A) A24-(α-ss-α)$_2$ has two $E_{m8.5}$ of -164 and -218 mV both with a standard deviation of 6 mV ($N = 2$). There is a reduced χ_v^2 of 0.0032 with probability $P_\chi \geq 0.99$ for the titration depicted. (B) Residuals of fraction heme reduced from a fit of the Nernst equation to two times $n = 1$ for A24 in 10 mM Tris-HCl buffer solution pH 8.5 (circles). For comparison, residuals for a single $n = 1$ Nernst fit with $E_{m8.5}$ of -190 mV (squares) show deviations near the midpoint characteristic of split $E_{m8.5}$. The dotted lines indicate limits of $\pm 5\%$.
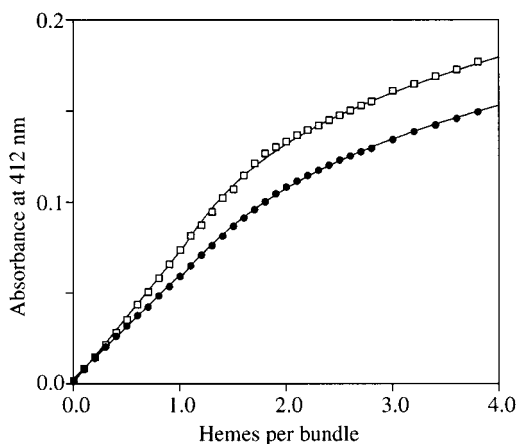
FIGURE 9: Binding titrations for ferric protoporphyrin XI with A24-(α-ss-α)$_2$ and S24-(α-ss-α)$_2$. The binding titrations shown were obtained with A24-(α-ss-α)$_2$ (closed circles) or S24-(α-ss-α)$_2$ (open squares) at 384 nM in 100 mM NaCl, 50 mM Tris-HCl buffer, pH 8.5 at 22 °C. The line fits to the points for A24-(α-ss-α)$_2$ is for two separate binding reactions of single hemes per bundle with a K_d values of 15 and 800 nM while the fit to the S24-(α-ss-α)$_2$ is for two hemes binding with the same K_d values of 5 nM. These values were established in titrations done over protein concentrations covering the range of K_d values.

Charge Interactions in Binding Titrations as a Probe for Syn- and Anti-Topology of A24-(α-ss-α)$_2$ and S24-(α-ss-α)$_2$. The charge interactions that specifically split the redox potentials of diheme A24-(α-ss-α)$_2$ but not diheme S24-(α-ss-α)$_2$ should lead to biphasic binding titrations of ferric hemes to A24-(α-ss-α)$_2$ but not S24-(α-ss-α)$_2$. Figure 9 shows sample binding titrations of ferric protoporphyrin IX titrations with A24-(α-ss-α)$_2$ and S24-(α-ss-α)$_2$. Titrations constructed at protein concentrations selected to optimize the determination of the two disparate affinities (not shown) reveal K_d values 10$-$20 nM for the first ferric heme bound

and 500$-$800 nM for the second heme bound, an approximately 25$-$80-fold difference. In the case of S24-(α-ss-α)$_2$, two hemes per (α-ss-α)$_2$ are bound with indistinguishable K_d values in the 5 nM range. These measurements confirm previous results on A24-(α-ss-α)$_2$ (*18*, *29*) and support the idea that there is charge repulsion to the second ferric-heme binding adjacent to the first in a essentially *syn*-topology of A24-(α-ss-α)$_2$. The absence of any splitting in the heme titrations of S24-(α-ss-α)$_2$ together with the finding that K_d values for both hemes are similar to the first heme binding to A24-(α-ss-α)$_2$ supports the conclusion drawn from the redox titrations that the hemes in S24-(α-ss-α)$_2$ are distal in a predominantly *anti*-topology. Results from redox titrations and binding titrations are summarized in Table 1.

Pendant Coproporphyrin (CP) as a Probe for Syn- and Anti-Topology of A24-(α-ss-α)$_2$ and S24-(α-ss-α)$_2$. As we have already mentioned, CP is recognized to promote *syn*-topology by an estimated 1.5$-$2.0 kcal/mol (*23*, *38*). Figure 10 shows spectra of A24-(CP-α-ss-α)$_2$ and S24-(CP-α-ss-α)$_2$ with no hemes present taken at various ionic strengths. In all cases, the spectra are nearly superimposable and dominated by a CP absorbance typical of the cofacial dimer (372 nm; see Figure 4). The *syn*-topology reported by CP for A24-(CP-α-ss-α)$_2$ is in agreement with all the other A24-(α-ss-α)$_2$ proteins examined, but the *syn*-topology found for S24-(CP-α-ss-α)$_2$ is in sharp contrast to the highly *anti*-topologies so far seen for other S24-(α-ss-α)$_2$ proteins. Thus, it is clear that pendant CP is capable of shifting the *anti*-*syn*-ratio from the ≥ 20, seen in S24-(pyr-α-ss-α)$_2$ and in the diheme S24-(α-ss-α)$_2$, to ≤ 0.05 as seen in S24-(CP-α-ss-α)$_2$. Hence, all other things being equal, the contribution from the CP dimerization itself to the over 400-fold shift in anti-*syn*-ratio will be ≥ 3.5 kcal/mol (eq 1a), a value substantially higher than the earlier estimates made under similar conditions (*23*, *24*, *38*).

Because of the propionate substituents on each CP, we again considered that lowering the solution ionic strength from the high values used so far would increase the repulsion between the charges on the CP, decrease the tendency of the CP to dimerize and hence shift the equilibrium toward an *anti*-topology. Moreover, because there are *three* anionic charges present upon each CP, it was reasonable to consider that some form of cooperative response might be displayed leading to a sharp dependency on ionic strength of the *anti*-*syn*-ratio. The inset of Figure 10 focuses on the part of the CP spectrum where the monomeric form will absorb reporting an *anti*-topology. Measurements on A24-(CP-α-ss-α)$_2$ at 50 and 10 mM Tris-HCl (spectra a and b) had no measurable effect on the *anti*-*syn*-ratios which remained at ≤ 0.05. However, S24-(CP-α-ss-α)$_2$ at the lower ionic strengths (spectra c$-$e) does display signs of a shift to longer wavelengths as the ionic strength is lowered, suggesting the inclusion of a small contribution of the CP monomer. Deconvolution of the low ionic strength spectra (not shown) indicates that the *anti*-topology fraction rose into the 0.05$-$0.1 range for 50 and 10 mM Tris-HCl.

Heme Binding and Heme Oxidation State Perturbations on the Anti-Syn-Ratio of S24-(CP-α-ss-α)$_2$, Demonstrating a Charge Activated Syn- to Anti-Topological Switch. The hint shown in Figure 10 that the anti-*syn*-ratio of S24-(CP-α-ss-α)$_2$ was just about at the measurable *anti*-threshold on the *syn*-side of the equilibrium at moderate and low ionic

Table 1: Redox Midpoints and Binding Affinities of Hemes in (α-ss-α)₂ Maquettes

maquette	ionic conc[a]	hemes/ maquette	heme oxidation−reduction					heme dissociation−binding				
			$E_{m8.5}$ (mV)[abc]		$\Delta G^{o\prime}_{redox}$ (kcal/mol)		$\Delta\Delta G^{o\prime}$ interaction redox	K_d (nM)		$\Delta G^{o\prime}_{diss-bind}$ (kcal/mol)		$\Delta\Delta G^{o\prime}$ interaction bind
			$K_{eq1}{}^d$	K_{eq3}	$K_{eq1}{}^d$	K_{eq3}		$K_{eq1}{}^e$	K_{eq3}	$K_{eq1}{}^e$	K_{eq3}	
A24	H	1		−159		3.7			10−20			
S24	H	1		−195		4.5			5			
A24	H	2	−170	−246	3.9	5.7	1.85	500 to 800	10−20	9.5 to 8.2	10.8 to 10.4	1.9 to 2.6
S24	H	2	−207	−207	4.8	4.8	0	5	5	11.2	11.2	0
A24	L	2	−164	−218	3.8	5.0	1.2					

[a] Midpoint potentials are given at pH 8.5 for 50 mM Tris-HCl buffer solution containing 100 mM NaCl (high ionic strength, H) except for the two heme A24 titration which was performed at 10 mM Tris-HCl buffer solution at pH 8.5, (low ionic strength, L) and ambient temperature. [b] The $E_{m8.5}$ values are some 30 mV lower than earlier published numbers for the A24-(α-ss-α)₂ measured under similar titration conditions. It appears that redox titrations done within an hour of heme addition (on a similar time scale as the heme binding reactions) give lower E_m values than titrations done after many hours as in earlier work. The difference may reflect an "annealing" of the heme-protein structures over time that leads perhaps to a more complete removal of interior water around the heme, loss of stabilization for the ferric form, and hence a rise in E_m value. [c] There is a difference in E_m values of hemes in the *syn*-A24-(α-ss-α)₂ and the *anti*-S24-(α-ss-α)₂. [d] Subscripts signify that the reactions are related to the equilibria K_{eq1} and K_{eq3} of Figure 1 and eq 1. The relationship between redox equilibria ($E_{m8.5}$) and $\Delta G^{o\prime}$ values is given in eq 3. [e] The K_d values are for ferric heme. Again, subscripts signify the relationship with K_{eq1} and K_{eq3} in Figure 1 and eq 1.
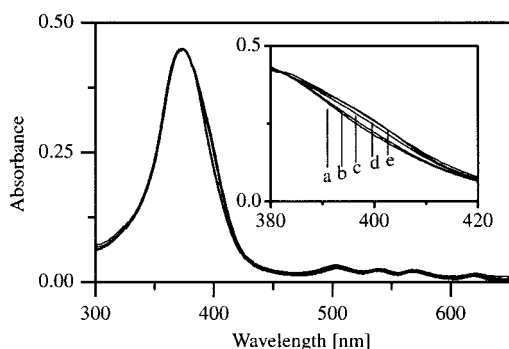
FIGURE 10: Comparison of absorbance spectra of *apo*-forms of A24-(CP-α-ss-α)₂ and S24-(CP-α-ss-α)₂ in buffers of various ionic strength. *Apo*-A24-(CP-α-ss-α)₂ is shown in buffers of (a) 50mM Tris-HCl, (b) 10 mM Tris-HCl, and S24-(CP-α-ss-α)₂ in (c) 100 mM NaCl, 50 mM Tris-HCl, (d) 50mM Tris-HCl, and (e) 10 mM Tris-HCl, all at pH 8.5 and ambient temperature. A24- and S24-(α-ss-α)₂ concentrations are 3−5 μM; the spectra are normalized for comparison. The CP-dimer peak is at 372 nm indicating a dominant *syn*-topology. The inset is an enlargement of the region around the 394 nm band. The shoulder in the absorbance spectrum of S24-(CP-α-ss-α)₂ in 10 mM Tris-HCl and in 50 mM Tris-HCl indicates the presence of CP-monomer at 394 nm.

strength sets the stage for precise measurements of the effect on the *anti-syn*-ratio of S24-(CP-α-ss-α)₂ by the introduction of one and two ferrous or ferric hemes. The *anti-syn*-ratio of S24-(CP-α-ss-α)₂ in 50 mM Tris-HCl buffer (pH 8.5) was first examined for response to steric perturbations arising from the introduction of the heme itself. For this, the formally neutral ferrous form was examined. Figure 11, panel A, shows the spectral changes to S24-(CP-α-ss-α)₂ in the absence of heme (a) and following the binding of one ferrous heme (b) and two ferrous hemes (c). It is clear from the spectra that the binding of one and two ferrous hemes causes no significant effect upon the CP spectrum which remains dominated by the CP dimer band at 372 nm. Deconvolution reveals that the *anti-syn*-ratio remains below 0.1 throughout. Such a result excludes significant steric hindrance and destabilization of the *syn*-topology resulting from heme coordination to S24-(CP-α-ss-α)₂.

Figure 11, panel B, shows the spectral changes upon addition to S24-(CP-α-ss-α)₂ of one and two cationic ferric hemes in 50 mM Tris-HCl buffer. As compared to the initial

spectrum a, there is a small alteration in the CP spectrum with the addition of one ferric heme (b). With the addition of a second heme (c), the CP band shifts from 372 to 394 nm, indicating a major transition from CP-dimer to monomer, which suggests a dominant *anti*-topology. Deconvolution of these spectra reveals that the *anti-syn*-ratio changes from 0.03 to 0.05 with no hemes present to 0.22 after one ferric heme is added per S24-(CP-α-ss-α)₂ and then to about 2.4 of the two ferric hemes added. The switch from *syn*-S24-(CP-α-ss-α)₂ to the *anti*-topology does not occur when two ferrous hemes are present, or when one ferric heme is present, but only when two ferric hemes are present. This strongly suggests that charge interactions between adjacent ferric hemes are primarily responsible for shifting S24-(CP-α-ss-α)₂ from the *syn*- to the *anti*-topology. Figure 11, panel C, shows that as expected, A24-(CP-α-ss-α)₂ does not display the CP spectral changes upon addition of ferric heme that was seen for S24-(CP-α-ss-α)₂. This suggests that the *anti-syn*-ratio is intrinsically too small to be shifted into the measurable range by any of the stimuli and conditions so far applied.

Figure 12 shows a closer examination of a heme titration to S24-(CP-α-ss-α)₂ until both heme-binding sites are occupied. Titration curve b generated at 50 mM Tris-HCl corresponds to the sample spectra presented in Figure 11, panel B. The pronounced dependency of the fraction in the *anti*-topology on the ionic composition of the bulk solution is revealed progressively in comparing titration a at 10 mM Tris HCl with titration b at 50 mM Tris HCl and titration c at the 100 mM NaCl, 50 mM Tris HCl. The course of the increase in *anti*-topology visible at the two lowest ionic strengths follows the statistical expectation of double occupancy of the S24-(CP-α-ss-α)₂ by two ferric hemes, and the data were readily fit as shown to the previously described model of double occupancy (*37*). Titration d emphasizes the specificity of the response to electrostatic repulsion between hemes, since even at the lowest ionic strength (10 mM Tris-HCl) adding ferrous heme to S24-(CP-α-ss-α)₂ presented little contribution from steric effects. And titration e emphasizes that addition of ferric hemes to A24-(CP-α-ss-α)₂ even at the lowest ionic strength had no significant effect. Thus, these measurements demonstrate a strict requirement
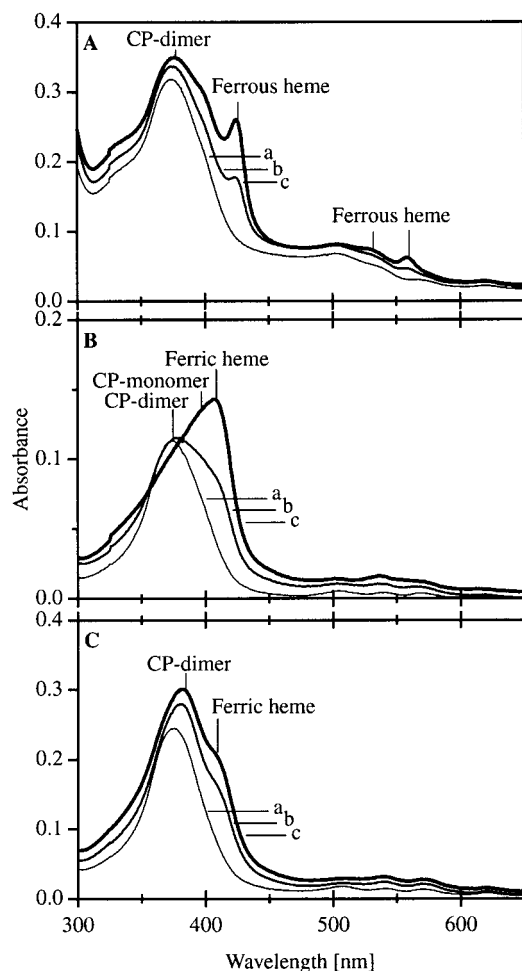
FIGURE 11: Effect of ferrous and ferric heme additions of S24-(CP-α-ss-α)$_2$ and A24-(CP-α-ss-α)$_2$. (A) Successive addition of (a) 0, (b) 1.2, and (c) 2.0 ferrous hemes per S24-(CP-α-ss-α)$_2$ in 50 mM Tris-HCl buffer with no NaCl, at pH 8.5 and ambient temperature. There is a CP-dimer band at 372 nm indicating *syn*-topology, and the ferrous-heme band is at 426 nm. (B) Successive addition of (a) 0, (b) 1.0, and (c) 2.0 ferric hemes per S24-(CP-α-ss-α)$_2$ in 50 mM Tris-HCl buffer at pH 8.5 at ambient temperature. There is a CP-dimer band at 372 nm indicating predominantly *syn*-topology for a and b, and there is a CP-monomer band is at 394 nm indicating predominantly *anti*-topology for c, and the ferric-heme band is at 411 nm. The final spectrum observed is after 40 min. (C) Successive addition of (a) 0, (b) 1.0, and (c) 2.0 ferric hemes per A24-(CP-α-ss-α)$_2$ in 50 mM Tris-HCl buffer at pH 8.5 at ambient temperature. The CP-dimer band at 372 nm indicates predominantly *syn*-topology, and the ferric-heme band is at 411 nm.

for the ligation of more than one, but no more than two, ferric hemes to the histidines at position 10,10′ in each subunit of S24-(CP-α-ss-α)$_2$ to elicit a reversible between the switch in *syn*- to *anti*-topological structures.

The dramatic effect of external ionic strength described in Figure 12 on the *anti-syn*-ratio of diferric-heme S24-(CP-α-ss-α)$_2$ reflects a type of electrostatic cooperativity in which the concentration of multiple negative charges on each CP profoundly alters the association between CP units (and hence the *anti-syn*-ratio) over a modest range of ionic strengths; similar effects have been observed for CP in aqueous solution (*40*). Further support that the principal component of the electrostatic interaction is the charged propionates on the CP comes from the observation that the K_d range of 2×10^{-5} to 2×10^{-8} M for CP dissociation in
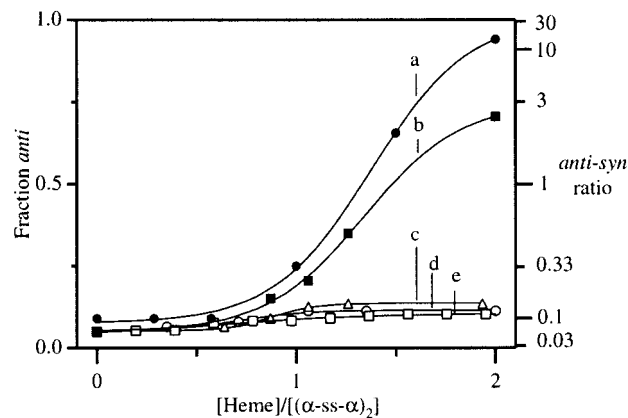
FIGURE 12: Heme titrations of A24-(CP-α-ss-α)$_2$ and S24-(CP-α-ss-α)$_2$. The fraction of *anti*-topology (left) or the *anti-syn*-ratio (right) is plotted against the number of hemes added per (CP-α-ss-α)$_2$ in various buffer solutions. Trace (a) is S24-(CP-α-ss-α)$_2$ titrated with ferric hemes in 10 mM Tris-HCl buffer (filled circles). Trace (b) is S24-(CP-α-ss-α)$_2$ titrated with ferric hemes in 50 mM Tris-HCl buffer (filled squares). The data of a and b are fitted to theoretical curves modeling the probability of double occupancy of hemes based upon the heme K_d values. Trace (c) is S24-(CP-α-ss-α)$_2$ titrated with ferric hemes in 100 mM NaCl, 50 mM Tris-HCl buffer (open squares). Trace (d) is S24-(CP-α-ss-α)$_2$ titrated with ferrous hemes in 50 mM Tris buffer (open circles) and trace (e) A24-(CP-α-ss-α)$_2$ with ferric hemes in 50 mM Tris-HCl buffer (open triangles). All solutions are at pH 8.5 and ambient temperature.

(CP-α-ss-α)$_2$ is closer to the K_d value for free CP in solution [2×10^{-6} M under similar conditions (*23*)] than to the bundle K_d (on the order of 10^{-12} M, F. Rabanal, unpublished measurement). This sensitivity of the external charges on the CP to the external ionic environment is in sharp contrast to the absence of such effects on the internal charge interactions occurring between the protein bound and the solvent-protected ferric hemes discussed above.

Summary of Equilibrium Constants and Free Energies. Table 1 presents the collected redox midpoint potentials ($E_{m8.5}$ values) and dissociation constants (K_d values) of one and two hemes in S24-(α-ss-α)$_2$ and its control companion A24-(α-ss-α)$_2$. Table 2 summarizes the topologies determined by the three different methods for the A24-(α-ss-α)$_2$ and S24-(α-ss-α)$_2$ series, and Table 3 presents the deduced $K_{anti-syn}$ and $\Delta G°\,'$ values for the *anti-syn*-equilibrium induced by ferric-heme binding or heme oxidation−reduction in S24-(CP-α-ss-α)$_2$.

Switch Kinetics. Preliminary work following the *anti-syn* topological switch kinetics after rapid oxidation or reduction shows a dramatic temperature dependence. For the maquettes described here, room temperature topological changes were on the several minutes time-scale. Thus, after the incubation time of 40 min following a pulse redox change, the reaction was nearly complete.

DISCUSSION

Proof of Principle. De novo designed synthetic proteins and maquettes become useful when in simplified structure they demonstrate "proof of principle" of biological engineering normally obscured within the multifunctional complexity of native proteins. The engineering principle we demonstrated in a simple homodimeric tetra-α-helix bundle is that of a conformational switch protein that moves back and forth

Table 2: Equilibrium Constants for the *Anti-Syn*-Ratio Obtained by Various Probes for $(\alpha\text{-SS-}\alpha)_2$ Protein Maquettes

hemes per $(\alpha\text{-ss-}\alpha)_2$	probe	ionic conc[a]	redox state of heme	$K_{anti-syn}$ $(\alpha\text{-ss-}\alpha)_2$[b] A24	S24
none	pyrene	L		≤1.00	≥12.5
	CP	L		≤0.03	0.11
	CP	M		≤0.03	0.05
	CP	M	reduced soln		0.03
	CP	H		≤0.03	0.04
one	CP	L	ferric		0.33[c]
	CP	M	ferric	0.10	0.22[c]
	CP	M	ferrous		0.07
	CP	H	ferric		0.07
two	E_m	L		≤0.05	
	E_m	H		≤0.05	≥20
	CP	L	ferric		19
	CP	M	ferric	0.13	2.39
	CP	M	ferrous		0.09
	CP	H	ferric		0.13

[a] Aqueous conditions, all at pH 8.5, are H, high ionic strength (100 mM NaCl, 50mM Tris-HCl buffer); M, moderate ionic strength (50 mM Tris-HCl buffer); and L, low ionic strength (10 mM Tris-HCl buffer). [b] Addition of ferrous or ferric heme slightly raises the absorbance at 392 nm and leads to a small overestimate of the level of anti-topology and the $K_{anti-syn}$ values according to our method (see Figure 12). For simplicity, corrections of this overestimate were not made. [c] These values obtained for one ferric heme present per $(\alpha\text{-ss-}\alpha)_2$ are significantly higher than those obtained in the absence of heme because of the statistical probability of there being two heme present (see Figure 12).

between two distinct states in response to a specific stimulus. The switch is a conspicuous transformation of the two subunits between *syn-* and *anti*-topology. The transformation includes structural changes in overall symmetry of the bundle and extensive alterations in surface patterns of the amino acids, some being displaced by as much as 4 nm. The driving stimulus of the switch is ferric-heme binding/release or heme redox changes that modulate internal charge interactions between the hemes. The maquette is engineered to couple and balance the forces of heme charge change and topological switch in a reversible and conserved manner. The energetics of the switch changes are in the 1.85−2.6 kcal/mol range. These energies are large enough to enable a stimulus to elicit a topological equilibrium change that would be biologically significant. Similar coupling processes appear in the engineering central to signaling, regulation, energy conversion, and chemical catalysis in natural proteins and enzymes. Moreover, the maquette proves that these simple protein scaffolds can also readily accommodate independent allosteric and cooperative regulation of the switch, modulated in this case by ionic strength. Such regulation shifts the *syn-* and *anti*-topological equilibrium out of functional energetic range of the stimulus, akin to allosterically regulated natural proteins.

Switch and Stimulus Action Involves Several Simple Two-State Transitions. If the switch between *syn-* and *anti*-topologies was heterogeneous and spread over multiple structural states, the heme binding and redox properties would be expected to be dispersed. Instead, as demonstrated by S24- and A24-$(\alpha\text{-ss-}\alpha)_2$ which remain fixed in *anti-* or *syn*-topology during the analysis, ferric-heme binding titrations and redox titrations display well-defined, homogeneous transitions. There is one binding step for two hemes binding to the *anti*-S24-$(\alpha\text{-ss-}\alpha)_2$, consistent with both hemes binding

to identical sites at opposite ends of the molecule, without significant charge interaction. In contrast, there are two binding steps for two hemes binding to the *syn*-A24-$(\alpha\text{-ss-}\alpha)_2$, consistent with a second heme bound more weakly than the first because it is opposed by the like charge on the adjacent bound first heme. Similarly, in analogous redox titrations, there is a single, >97% homogeneous transition for both hemes in the *anti*-diheme S24-$(\alpha\text{-ss-}\alpha)_2$ and two clear split transitions for the hemes of the *syn*-form diheme A24-$(\alpha\text{-ss-}\alpha)_2$ due to redox charge repulsion. Moreover, in Figure 12, the course of the change in the *anti-syn*-equilibrium in S24-$(\text{CP-}\alpha\text{-ss-}\alpha)_2$ with varying ferric-heme concentration strongly suggests that the protein conformational change is also a two-state transition.

Switch Stimulus Specific for Two Internal Charges. S24-$(\text{CP-}\alpha\text{-ss-}\alpha)_2$ demonstrates a sharply specific requirement for the presence of two cationic ferric hemes to activate the *syn*-to *anti*-topological switch. Remarkably, there are little or no accompanying steric effects on the *anti-syn*-ratio from binding one or two formally uncharged ferrous-heme molecules or from binding a single cationic ferric heme (Figure 12). It seems clear that the charge repulsive effects that drive the switch are specifically those originating on the two adjacent ferric hemes acting across the interface of the α-ss-α subunits within the low dielectric medium of the $(\alpha\text{-ss-}\alpha)_2$ bundle.

It is unlikely that the propionate groups of the hemes in four-helix bundles, which resonance Raman shows remain ionized and negatively charged in this pH range (*29*), contribute much to the electrostatic repulsion. The bundles are sufficiently thin that these propionates can easily extend into the high dielectric constant region of the aqueous phase, which minimizes their contribution to the electric field at the heme (*29*).

Switch Stimulus Energetics. Table 1 summarizes the energetic magnitude of the charge interaction between adjacent hemes determined from the ferric-heme binding and redox splitting. Charge interactions are reflected in both the 25−80-fold difference in the K_d values of the first and second ferric heme bound and the ∼80 mV splitting of the redox potentials in the firmly *syn*-diheme A24-$(\alpha\text{-ss-}\alpha)_2$. Because there are little or no measurable differences in the K_d values or redox splitting in the firmly *anti*-diheme S24-$(\alpha\text{-ss-}\alpha)_2$, we take the binding difference or redox splitting to provide the free energy difference available to drive the switch, that is 1.9−2.6 or 1.85 kcal/mol, respectively. The redox splitting proved to be unaffected by the supporting salt and buffer (from 10 mM Tris-HCl to 150 mM NaCl, 50 mM Tris-HCl), demonstrating that the maquette structure isolates the charge interactions between the hemes across the subunits from the ionic composition of the external medium. This proves to be a critical part of the engineering of the switch.

Balancing and Matching Topological Switch and Stimulus Energetic Equilibria. Tables 2 and 3 summarize the *anti-syn*-ratios measured by different methods and determine the heme stimulated switch energetics. An effective switch requires an appropriate balancing of the poise between the two switch states and the energetic magnitude of the switch stimulus. Energetic mismatching and imbalance of the *anti-syn*-topological equilibrium with the charge repulsion was obvious in the early exploratory phases of this investigation. The *anti-syn*-ratio of the various *apo-* and ferrous-heme A24-$(\alpha\text{-ss-}\alpha)_2$ structures was too small to measure ($K_{anti-syn}$ <

Table 3: Equilibrium Constants and $\Delta G^{o\prime}$ Values for Heme Redox and Ferric-Heme Binding Induced Shifts in the *Anti-Syn*-Equilibrium in S24-(CP-α-ss-α)$_2$[a]

heme oxidation−reduction					heme dissociation-binding				
$K_{anti-syn}$[b]		$\Delta G^{o\prime}_{anti-syn}$ (kcal/mol)		$\Delta\Delta G^{o\prime}_{switch}$	$K_{anti-syn}$[b]		$\Delta G^{o\prime}_{anti-syn}$ (kcal/mol)		$\Delta\Delta G^{o\prime}_{switch}$
K_{eq4}	K_{eq2}	K_{eq4}	K_{eq2}	(kcal/mol)	K_{eq4}	K_{eq2}	K_{eq4}	K_{eq2}	(kcal/mol)
2 ferrous hemes	2 ferric hemes	2 ferrous hemes	2 ferric hemes	2 ferric minus 2 ferrous	0 hemes	2 ferric hemes	0 hemes	2 ferric hemes	2 ferric minus no hemes
0.09	2.39	1.41	−0.51	1.92	0.05	2.39	1.75	−0.51	2.26

[a] At moderate ionic strength, 50 mM Tris-HCl, pH 8.5. [b] The small overestimate of $K_{anti-syn}$ in heme containing maquettes (see footnote *c* of Table 2) contributes to an estimate of $\Delta\Delta G^{o\prime}_{switch}$ redox which is less than $\Delta\Delta G^{o\prime}_{switch}$ binding.

0.05) suggesting that a $\Delta\Delta G^{\circ\prime}_{interaction}$ of at least 4 kcal/mol would be required to drive the $K_{anti-syn} > 10$. The $\Delta\Delta G^{\circ\prime}_{interaction}$ provided by the diferric-heme repulsion (1.85 to 2.6 kcal/mol) falls well short of this requirement. In contrast, the *apo-* and ferrous-heme S24-(α-ss-α)$_2$ structures were already in the switched *anti*-topology ($K_{anti-syn} > 100$), and hence a diferric-heme S24-(α-ss-α)$_2$ state would be expected to move to even higher *anti-syn*-ratios. Neither of these cases yield the gross change in structural populations required to function as a switch.

However, we used the tendency of CP to form cofacial dimers [adding a >3.6 kcal/mol shift toward the *syn*-topology of any (α-ss-α)$_2$] to alter the balance. While the incorporation of CP exacerbates the nonfunctional switch status of diheme A24-(α-ss-α)$_2$, CP draws diheme S24-(CP α-ss-α)$_2$ toward the functional threshold. Indeed, at the highest ionic strength (100 mM NaCl, 50 mM Tris-HCl), CP in S24(CP α-ss-α)$_2$ establishes too strong a *syn*-dominance [$K_{anti-syn} < 0.05$ even in the diferric-heme S24-(CP α-ss-α)$_2$]. At lower ionic strengths, CP dimer formation is just strong enough to bring the *anti-syn*-equilibrium to the working threshold. Thus at <50 mM Tris-HCl, the initial *syn-anti*-ratio is poised on the correct *syn*-side of the equilibrium ($K_{anti-syn}$ 0.05 to 0.1), permitting a $\Delta\Delta G^{\circ\prime}_{interaction}$ value in the 1.85 to 2.6 kcal/mol range to drive a 50 to 80-fold topology switch to effect the desired conspicuous change in the populations of the *anti-syn*-topologies.

The switch works in this way: at equilibrium at low ionic strengths, S24-(CP-α-ss-α)$_2$ and its diferrous- and monoferric-heme forms favor a resting topology suitably dominated by the *syn*-topology, but the charge repulsion in the diferric-heme S24-(CP-α-ss-α)$_2$ drives the protein structure from this favored, resting, predominantly *syn*-topology into an unfavored, tense, predominantly *anti*-topology balanced against the force evident between the two cationic hemes. Removal of this force by heme reduction or association permits tension in the *anti*-topology to spontaneously drive the structure back to the resting *syn*-topology. These reactions are summarized in the equilibrium scheme of Figure 13.

Function and Specificity as a Sensor and Signal Protein Maquette. The single heme S24-(CP-α-ss-α)$_2$ is poised on the threshold of the *syn-* to *anti*-transition and can perform as a sensor of solution ferric heme. Likewise, the diferrous-heme S24-(CP-α-ss-α)$_2$ is similarly poised to perform as a sensor of solution oxidants that interact with the two hemes in situ. These two forms of sensing are coupled to a common conformational switch as summarized in the scheme of Figure 13.

We can view their performance as sensors and signaling protein maquettes much as we might a natural counterpart.

A substantial contribution to heme binding affinity and specificity is provided by the bis-histidine axial ligation of the hemes. In the absence of histidines, otherwise identical (α-ss-α)$_2$ proteins simply partition the substantially hydrophobic hemes and other porphyrins out of the water into the interior of the bundle with apparent K_d values in the 100 μM range (ref *41*; K. S. Reddy, unpublished observations). Thus, in the present maquettes which display heme K_d values in the 1−10 nM range, axial histidine ligation appears to contribute 5−6 kcal/mol of binding free energy above the partitioning threshold for nonligated porphyrin structures. However, this axial ligation is not restricted to hemes. Hence, the presence of other metalloporphyrins will alter the performance of switch action. For instance, histidine-containing (α-ss-α)$_2$ proteins bind Zn and Mg protoporphyrins (*42*) and hemes A (*43*) at higher affinities (K_d values < 5 nM) than that of the iron protoporphyrin IX (hemes B) used in the present study. Moreover, it is likely that farnesyl tail of heme A would for steric reasons promote the *anti*-topology independent of the redox state of the heme (*43*). In contrast, the binding of redox inactive, formally neutral, Zn and Mg protoporphyrin are likely to competitively abolish any charge-driven conformational response and return the structure to its favored *syn*-topology. From the biochemical view, each of these molecules would be regarded as competitive inhibitors of the maquette switch activity.

The equilibrium redox midpoint potential values of the hemes determine which redox agents can or cannot drive the switch from *syn-* to *anti*-topology and back. For example, if the hemes are initially reduced and the maquette structurally relaxed in the *syn*-topology, the switch will be readily activated by an oxidant with an $E_{m8.5}$ value > -150mV. Both the first heme ($E_{m8.5}$ value -250mV) and second heme ($E_{m8.5}$ value -150 mV) will be oxidized before the structure is driven to the *anti*-topology where the $E_{m8.5}$ values are similar at -210mV. The reverse process is driven by reductants with $E_{m8.5}$ value < -210 mV. The present design is poised to work reversibly with superoxide/dioxygen couple ($E_{m8.5} \sim -200$mV) in a manner that may occur in the iron sulfur clusters of the superoxide signaling system SoxR (*44, 45*). Indeed, a closely related member of the first generation prototype, H10H24-(α-ss-α)$_2$ containing hemes A and B catalyzes rapid oxidation by dioxygen and reduction by NADH via by diaphorase (*43*). Maquette heme redox midpoints can been modulated to shift the redox sensitive range (*29, 46*).

Allosteric Regulation. Ionic strength has a minimal effect on the splitting of the redox potentials and hence the repulsive force between the adjacent ferric hemes, indicating that the hemes are structurally protected from ionic influence of the
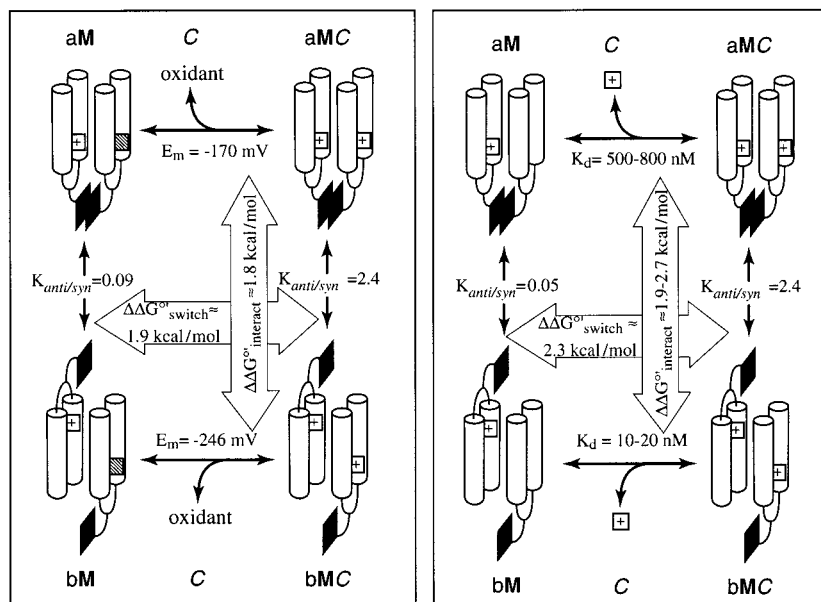
FIGURE 13: Summary of heme redox and heme binding induced-switch between *syn*- and *anti*-topological states of S24-(CP-α-ss-α)$_2$. The figure combines the equilibria of Figure 1, the *anti*- and *syn*-topologies of Figure 2, and the data of Tables 1−3. The general notation for a, b, **M**, and *C* come from Figure 1. Measures of the heme oxidation−reduction or ferric-heme binding-dissociation equilibria are given by the $E_{m8.5}$ values (left) and K_d values (right) which are related to the K_{eq1} and K_{eq3} of Figure 1 and Table 1. The $E_{m8.5}$ and K_d values presented are those revealed in CP-free A24-(α-ss-α)$_2$ because it is fixed in the *syn*-topology. Top and bottom row values reflect the splitting in the E_m and K_d, which provide two ways of evaluating the $\Delta\Delta G°'_{interaction}$ shown in the respective vertical broad arrows. The $K_{anti-syn}$ values are from S24-(CP-α-ss-α)$_2$ in the absence or presence of two ferric hemes are related to the K_{eq4} and K_{eq2}, respectively. $K_{anti-syn}$ values (related to K_{eq4}) for the single ferric heme (right) and one ferrous-ferric heme (left) per (α-ss-α)$_2$ taken to be the same as $K_{anti-syn}$ values observed for zero hemes and in the presence of two ferrous hemes per (α-ss-α)$_2$. This is reasonable since in the case of the binding titration the theoretical line in Figure 12 describing the statistical populations of substoichiometric ferric heme or ferric/ferrous heme populations extrapolates to the value observed at zero heme or two ferrous-heme S24-(CP-α-ss-α)$_2$. The broad horizontal arrows present the $\Delta\Delta G°'_{switch}$ values obtained from the splitting of the associated shifts in $K_{anti-syn}$ equilibrium constants.

aqueous phase. In sharp contrast, ionic strength modulates the charge interactions between the external CPs with greatly enhanced sensitivity afforded by a type of electrostatic cooperativity between the two sets of their three carboxylates. This means that the switch action can be inactivated or activated by environmental ionic composition acting on the remotely placed CP dimer by moving the thermodynamic matching between charge interaction and *anti-syn*-topology into and out of energetic range. A similar allosteric regulation is likely to be affected by environmental pH changes that either neutralize the CP carboxylates and inactivate the switch, or deprotonate the carboxylates and activate the switch. Such regulations are analogous to the allosteric regulation of bis-phosphoglycerate on the oxy-deoxyheme transition of hemoglobin or lactose on the binding affinity of the lac repressor for its DNA binding domain.

The Nature of the Supporting Protein Structures. The primary sequences of the (α-ss-α)$_2$ proteins used to construct the maquette and its reference structures are closely related to the first generation prototype H10A24 (*18*). The primary sequence secures firm α-helical secondary structures in both the α-ss-α subunits and in both topological states of the (α-ss-α)$_2$ quaternary structure. The subunits that constitute the (α-ss-α)$_2$ quaternary structure are strongly associated, for example the measured K_d value of A24-(CP-α-ss-α)$_2$ is about 10^{-12} M (F. Rabanal, unpublished measurement). Typical guanidinium-HCl denaturation of this (α-ss-α)$_2$ family reveal satisfactory cooperative curves ($m = 2-3$) and high stabilities ($\Delta G°_{H_2 0}$ values of 15−25 kcal/mol) (*47*). CD spectroscopy reveals little difference in the secondary α-helical structures whether the subunits are in *syn*- or *anti*-topology. In either

form, they are water soluble with proven hydrophobic interior (*20, 38, 48, 49*).

NMR spectra of some *apo*-maquettes show a high level of conformational specificity indicative of a singular tertiary structure (*50−52*), i.e., specific interactions between amino acid side chains. However, NMR examination for tertiary structures of A24 or S24-(α-ss-α)$_2$ either without or with heme indicates that either the structures are subject to motion between multiple states on the millisecond time scale, or they exist in a static distributed population of distinctly different folded states. Nevertheless, there is evidence that the overall tetra-α-helix structure is sufficiently well-developed to yield several signs of tertiary structural homogeneity regarding the heme binding and its in situ properties. Histidine positions are narrowly specific to the internal 10 and 10′ of each α-ss-α subunit which promote heme K_d values of 1−10 nM (*47*). Other than binding at the 24,24′ positions identically placed four full turns away, binding is sharply weakened at other positions to fall below the measurable limit ($K_d > 200\ \mu$M), reflecting the loss of 5−6 kcal/mol contributed by bis-histidine ligation. Likewise, when two hemes are bound adjacently in *syn*-topology, the binding affinities demonstrate strict specificities for heme peripheral substituents describing heme−heme contact within the bundle interior (*20*). Moreover, glutamates at position 11 appear drawn into the bundle as part of the packing around bound heme, since the glutamate pK is 7 when the heme is the neutral ferrous state and 4.2 when in the cationic ferric state, a shift equivalent to 3.5 kcal/mol (*29*). At intervening pH values, the glutamate mediates proton exchange coupled with heme oxidation−reduction (1.0 H$^+$/heme). Thus despite the absence of a

singular tertiary structure for the side-chains within the tetra-α-helical structure, heme binding and oxidation−reduction and the topological shifts display homogeneous two-state transitions that drive several substantial complementary and opposing energetic interactions from different parts of the protein.

REFERENCES

1. Perutz, M. F., Wilkinson, A. J., Paoli, M., and Dodson, G. G. (1998) *Annu. Rev. Biophys. Biomol. Struct. 27*, 1−34.
2. Kercher, M. A., Lu, P., and Lewis, M. (1997) *Curr. Opin. Struct. Biol. 7*, 76.
3. Sauer, R. T. (1996) *Structure 4*, 219−22.
4. Steitz, T. A., Harrison, R., Weber, I. T., and Leahy, M. (1983) *Ciba Found. Symp. 93*, 25−46.
5. Stock, D., Leslie, A. G. W., and Walker, J. E. (1999) *Science 286*, 1700−1705.
6. Junge, W. (1999) *Proc. Natl. Acad. Sci. U.S.A. 96*, 4735−4737.
7. Iwata, S., Lee, J. W., Okada, K., Lee, J. K., Iwata, M., Rasmussen, B., Link, T. A., Ramaswamy, S., and Jap, B. K. (1998) *Science 281*, 64−71.
8. Zhang, Z., Huang, L., Shulmeister, V. M., Chi, Y. I., Kim, K. K., Hung, L. W., Crofts, A. R., Berry, E. A., and Kim, S. H. (1998) *Nature 392*, 677−684.
9. Kim, H., Xia, D., Yu, C.-A., Xia, J.-Z., Kachurin, A. M., Zhang, L., Yu, L., and Deisenhofer, J. (1998) *Proc. Natl. Acad. Sci. U.S.A. 95*, 8026−8033.
10. Darrouzet, E., Valkova-Valchanova, M., Moser, C. C., Dutton, P. L., and Daldal, F. (2000) *Proc. Natl. Acad. Sci. U.S.A. 97*, 4567−4572.
11. Iwata, S., Kamata, K., Yoshida, S., Minowa, T., and Ohta, T. (1994) *Nat. Struct. Biol. 1*, 176−185.
12. Lewis, M., Chang, G., Horton, N. C., Kercher, M. A., Pace, H. C., Schumacher, M. A., Brennan, R. G., and Lu, P. Z. (1996) *Science 271*, 1247−1254.
13. DeRosier, D. J. (1998) *Cell 93*, 17−20.
14. DeGrado, W. F., Wasserman, Z. R., and Lear, J. D. (1989) *Science 243*, 622−628.
15. Hodges, R. S. (1996) *Biochem. Cell Biol. 74*, 133−54.
16. Betz, S. F., Bryson, J. W., and DeGrado, W. F. (1995) *Curr. Opin. Struct. Biol. 5*, 457−463.
17. Adamson, J. G., Zhou, N. E., and Hodges, R. S. (1993) *Curr. Opin. Biotech. 4*, 428−37.
18. Robertson, D. E., Farid, R. S., Moser, C. C., Urbauer, J. L., Mulholland, S. E., Pidikiti, R., Lear, J. D., Wand, A. J., DeGrado, W. F., and Dutton, P. L. (1994) *Nature 368*, 425−432.
19. Grosset, A. M., Rabanal, F., Farid, R. S., Robertson, D. E., Pilloud, D. L., DeGrado, W. F., and Dutton, P. L. (1995) in *Fourteenth American Peptide Symposium* (Kaumaya, P. T. P., Hodges, R. S., Eds.) pp 573−574, Mayflower Scientific, Ltd., England, Columbus, OH.
20. Kalsbeck, W. A., Robertson, D. E., Pandey, R. K., Smith, K. M., Dutton, P. L., and Bocian, D. F. (1996) *Biochemistry 35*, 3429−3438.
21. Pilloud, D. L., Rabanal, F., Gibney, B. R., Farid, R. S., Dutton, P. L., and Moser, C. C. (1998) *J. Phys. Chem. B 102*, 1926−1937.
22. Betz, S. F., and DeGrado, W. F. (1996) *Biochemistry 35*, 6955−6962.
23. Rabanal, F., DeGrado, W. F., and Dutton, P. L. (1996) *J. Am. Chem. Soc. 118*, 473−474.
24. Rabanal, F., Gibney, B. R., DeGrado, W. F., Moser, C. C., and Dutton, P. L. (1996) *Inorg. Chim. Acta 0243*, 213-218.
25. Rabanal, F., DeGrado, W. F., and Dutton, P. L. (1996) *Tetrahedron Lett. 37*, 1347−1350.
26. Creighton, T. E. (1993) in *Proteins: Structures and Molecular Properties*, pp 14−17, W. H. Freeman and Co., New York.
27. Garcia-Echeverria, C. (1994) *J. Am. Chem. Soc. 116*, 6031−2.
28. Gibney, B. R., Rabanal, F., Reddy, K. S., and Dutton, P. L. (1998) *Biochemistry 37*, 4635−4643.
29. Shifman, J. M., Moser, C. C., Kalsbeck, W. A., Bocian, D. F., and Dutton, P. L. (1998) *Biochemistry 37*, 16815.
30. Dutton, P. L. (1978) *Methods Enzymol. 54*, 411−35.
31. Turro, N. J. (1991) in *Modern Molecular Photochemistry*, pp 141−143, 105−106, University Science Books, Mill Valley, CA.
32. Birks, J. B. (1975) in *Organic Molecular Photophysics* (Birks, J. B., Ed.) pp 494−498, 505−508, John Wiley & Sons, New York.
33. Lehrer, S. S. (1997) *Methods Enzymol. 278*, 286−295.
34. Kaback, H. R., Jung, K., Jung, H., Wu, J., Prive, G. G., and Zen, K. (1993) *J. Bioenerg. Biomembr. 25*, 627−636.
35. Jung, K., Jung, H., Wu, J., Prive, G. G., and Kaback, H. R. (1993) *Biochemistry 32*, 12273−12278.
36. Sakamoto, S., Ueno, A., and Mihara, H. (1998) *J. Chem. Soc.-Perkin Transactions 2*, 2395−2404.
37. Daugherty, D. L., and Gellman, S. H. (1999) *J. Am. Chem. Soc. 121*, 4325−4333.
38. Gibney, B. R., Johansson, J. S., Rabanal, F., Skalicky, J. J., Wand, A. J., and Dutton, P. L. (1997) *Biochemistry 36*, 2798−2806.
39. Gunner, M. R., and Honig, B. (1991) *Proc. Natl. Acad. Sci. U.S.A. 88*, 9151−9155.
40. Morales-Rojas, H., and Yatsimirsky, A. K. (1999) *J. Phys. Org. Chem. 12*, 377−387.
41. Choma, C. T., Lear, J. D., Nelson, M. J., Dutton, P. L., Robertson, D. E., and DeGrado, W. F. (1994) *J. Am. Chem. Soc. 116*, 856−865.
42. Sharp, R. E., Diers, J. R., Bocian, D. F., and Dutton, P. L. (1998) *J. Am. Chem. Soc. 120*, 7103−7104.
43. Gibney, B. R., Isogai, Y., Reddy, K. S., Rabanal, F., Grosset, A. M., Moser, C. C., and Dutton, P. L. (2000) *Biochemistry 39*, 11041−11049.
44. Hidalgo, E., Ding, H., and Demple, B. (1997) *Trends Biochem. Sci. 22*, 207−10.
45. Ding, H., Hidalgo, E., and Demple, B. (1996) *J. Biol. Chem. 271*, 33173−5.
46. Shifman, J. M., Gibney, B. R., Sharp, R. E., and Dutton, P. L. (2000) *Biochemistry 39*, 14813−14821.
47. Gibney, B. R., and Dutton, P. L. (1999) *Protein Sci. 8*, 1888−1898.
48. Johansson, J. S., Gibney, B. R., Rabanal, F., Reddy, K. S., and Dutton, P. L. (1998) *Biochemistry 37*, 1421−1429.
49. Gibney, B. R., and Dutton, P. L. (2001) in *Adv. Inorg. Chem.* (Mauk, A. G., and Sykes, A. G., Eds.) pp 409−455, Academic Press, New York.
50. Skalicky, J. J., Gibney, B. R., Rabanal, F., Bieber-Urbauer, R. J., Dutton, P. L., and Wand, A. J. (1999) *J. Am. Chem. Soc. 121*, 4952−4960.
51. Gibney, B. R., Rabanal, F., Skalicky, J. J., Wand, A. J., and Dutton, P. L. (1999) *J. Am. Chem. Soc. 121*, 4952−4960.
52. Walsh, S. T., Cheng, H., Bryson, J. W., Roder, H., and DeGrado, W. F. (1999) *Proc. Natl. Acad. Sci. U.S.A. 96*, 5486-5491.